Available online at www.sciencedirect.com
SCIENCE DIRECT
Tectonophysics 415 (2006) 203–223
TECTONOPHYSICS
www.elsevier.com/locate/tecto

Evidence for lithospheric detachment in the central Andes from local earthquake tomography

B. Schurr [a,*,1], A. Rietbrock [b], G. Asch [c], R. Kind [c], O. Oncken [c]

[a] CTBTO, Wagramerstr. 5, PO BOX 1200, A-1400 Vienna, Austria
[b] University of Liverpool, Department of Earth and Ocean Sciences, 4 Brownlow Street, Liverpool L69 3GP, United Kingdom
[c] GeoForschungsZentrum Potsdam, Telegrafenberg, D-14473 Posdam, Germany

Received 19 May 2005; received in revised form 20 November 2005; accepted 20 December 2005
Available online 28 February 2006

Abstract

Data from three temporary seismic networks were merged for tomographic inversion. Although the deployments did not coincide in time, spatial overlap was achieved by re-occupying existing sites. Travel times and t^* operators of about 1600 earthquakes were inverted for 3D models of v_p, v_p/v_s and P-wave attenuation (Q_p^{-1}). All three attributes provide a consistent image of the entire subduction zone on a lithospheric scale. The tomographic images reveal low velocities and high attenuation in the crust and mantle underlying the Western Cordillera and most of the Puna plateau, indicative of weak rheology and mostly asthenospheric mantle. In contrast, forearc and eastern foreland are characterized by high Q_p values, corresponding to cold temperatures in accordance with thermal models. In the backarc, between 23°S and 24°S, a high velocity, high Q_p structure beneath the Eastern Cordillera and eastern Puna is interpreted as detaching continental lithosphere that has been thickened in the orogenic process. South of this structure, the mantle is characterized by low velocities, high v_p/v_s ratios, and low Q_p values. Here it is believed that lithosphere originally underlying Andean crust has already been removed. This is supported by new estimates of crustal thickness and volcanic activity.
© 2006 Elsevier B.V. All rights reserved.

Keywords: Tomography; Central Andes; Puna; Plateau building; Lithospheric detachment; Seismology

1. Introduction

The Andes have formed in a complex interaction of subduction-related and tectonic processes. In the central Andes, convergence of the oceanic Nazca and continental South American plates generated the Altiplano–Puna high plateau, the second largest continental plateau on earth. This is remarkable and puzzling, as most other regions that have been extensively uplifted are associated with collision of two buoyant continental plates, in which case crustal thickening and uplift is more intuitive. Different mechanisms have been suggested to explain the uplift of the Andean plateau: Magmatic addition, tectonic shortening, lithospheric thinning and hydration of mantle rocks (Giese et al., 1999). Due to its location above a subduction zone and associated abundant volcanism, plateau formation was originally

* Corresponding author. Tel.: +43 1 26030 6443; fax: +43 1 26030 5874.
E-mail addresses: bernd.schurr@ctbto.org (B. Schurr), ariet@liverpool.ac.uk (A. Rietbrock), asch@gfz-potsdam.de (G. Asch), kind@gfz-potsdam.de (R. Kind), oncken@gfz-potsdam.de (O. Oncken).
[1] Formerly GeoForschungsZentrum Potsdam, Germany.

0040-1951/$ - see front matter © 2006 Elsevier B.V. All rights reserved.
doi:10.1016/j.tecto.2005.12.007

attributed to magmatic processes (James, 1971). However, in order to explain crustal thickness by magmatic addition, unrealistically large amounts of igneous rocks would be necessary. Analysis of Neogene deformation on the eastern margin of the plateau led to models that rely mostly on tectonic shortening and lithospheric thinning to explain crustal thickness and average elevation (Isacks, 1988; Hindle et al., 2005).

An unsettled question in geodynamics is the role of the mantle lithosphere in mountain building. It is obvious that if crust is shortened, the underlying mantle lithosphere must shorten and thicken too. Surprisingly, thin lithosphere is often found beneath plateaus (e.g. northern Tibet). In the central Andes, along-strike variation of lithospheric thickness has been postulated by a regional study of seismic Q (Whitman et al., 1992). Apparently, the Altiplano has a significantly deeper lithospheric root than the more southern Puna (Haberland et al., 2003). The absence of recent backarc volcanism in the Altiplano and the succession of shoshonitic to calc–alkaline to ocean-island-basalt-type lavas from the northern to southern Puna have also been taken as evidence for southward lithospheric thinning (Kay et al., 1994). The change in lithospheric structure is accompanied by a major change in morphology: at around 22°S, the relatively flat Altiplano gives way to the more rugged, almost 1 km higher, Puna (Whitman et al., 1996). The causes of these quite fundamental structural differences are not understood.

In this study, we present a tomographic model of P-wave velocity, v_p/v_s ratio, and P-wave attenuation for the southern central Andes. We have merged data from the three temporary seismic deployments PISCO'94, ANCORP'96, and PUNA'97 to obtain a consistent model for the entire subduction zone at lithospheric scale. The PISCO and ANCORP data have been analyzed previously. Graeber and Asch (1999) presented a 3D v_p and v_p/v_s model for the forearc and western arc from PISCO travel time data. This was extended to the north with ANCORP data by Rietbrock and Haberland (1998). PISCO and ANCORP P-wave spectra were used for a 3D attenuation model by Haberland and Rietbrock (2001). Now all these data are combined and supplemented by data from the PUNA network (Schurr et al., 1999) that extended coverage of the PISCO and ANCORP experiments to the east, across the recent magmatic arc and into the backarc plateau of the Argentine Puna, completing an important part in the Andean structural puzzle. In addition to the new terrain of the backarc region, it also opened up the important eastern edge of the PISCO network, the Western Cordillera, by its overlapping set-up. This region could only partly be resolved before (Graeber and Asch, 1999; Haberland and Rietbrock, 2001). The Q_p model from all three deployments has already been interpreted by Schurr et al. (2003) with respect to fluid and melt transport. The limited region of the Atacama basin in the forearc has been analysed using all three parameters by Schurr and Rietbrock (2004). Thus in this paper, although the model comprises the entire subduction zone, discussion of results will be focused on those parts that are new and have not been analysed before, i.e. mainly the Western Cordillera and the Argentine backarc region.

2. Geology and tectonics

The Andes exhibit significant along- and across-strike variation in tectonic style, uplift history, and magmatism. Our study area lies in the central Andes between 20°S and 25°S, south of the prominent bend in the South American coastline (Fig. 1). Here, the Nazca plate subducts with a moderate dip of ~30° at a convergence rate of 65 mm/year (Angermann et al., 1999). The continental margin is composed of several major, mostly trench-parallel morpho-tectonic units. The forearc is stamped by the progressive eastward migration of volcanic arcs since the Jurassic. The Western Cordillera (WC) is the present volcanic front with its Miocene to recent strato-volcanoes, including the world's highest active volcano (Mt. Llullaillaco, 6723 m). The backarc consists of a high plateau, the Miocene fold and thrust belt of the Eastern Cordillera (EC), and a compressional foreland. The high plateau is divided into the Altiplano of Peru and Bolivia in the north and the Argentine Puna in the south. The Altiplano is an internally drained basin with an average elevation of ~3800 m and little topography, confined by the Western and Eastern Cordilleras. The Puna is characterized by a more rugged relief and higher average elevation enclosing a series of internally drained basins. The forelands of both plateau segments differ in deformational style: East of the Altiplano, the Subandean Ranges form an active thin-skinned fold and thrust belt. East of the Puna, in the Santa Barbara Ranges, deformation also involves basement rocks. The transition between these two segments occurs between approximately 22°S and 23°S. Plateau uplift began first in the Altiplano (~25 Ma) and later in the Puna (~15 Ma) (Gregory-Wodzicki, 2000). Magnitude of horizontal shortening continuously decreases from the center of the Altiplano towards the southern Puna (Kley and Monaldi, 1998).

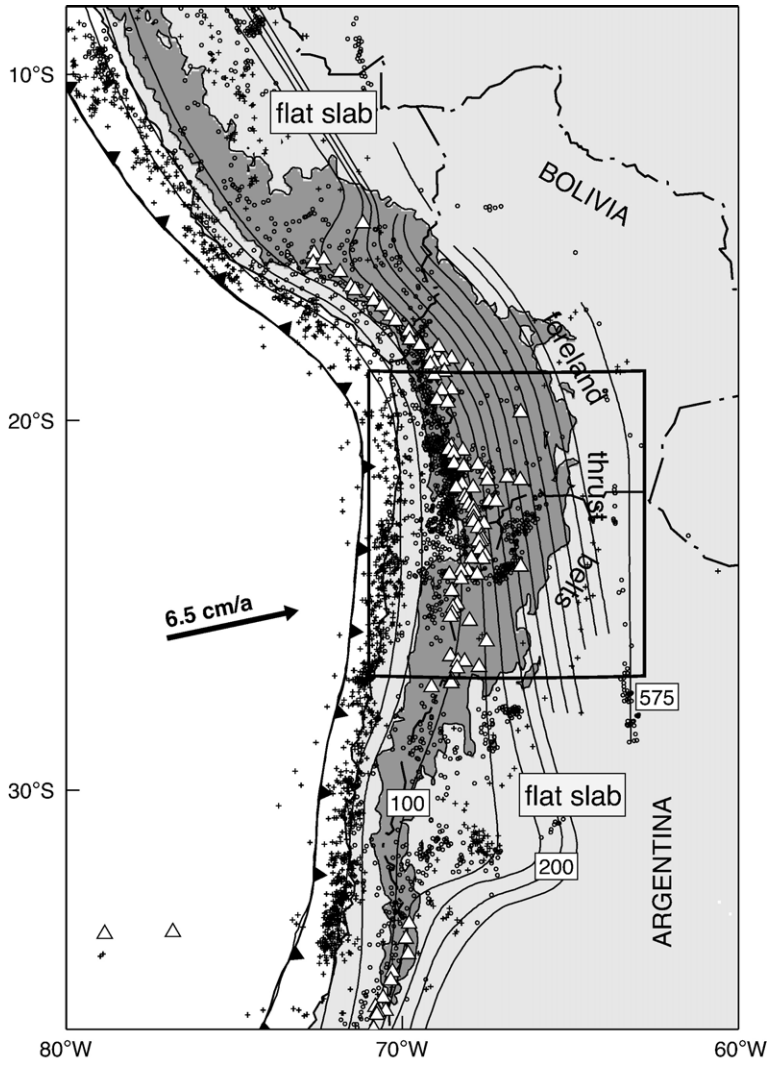

Fig. 1. Overview of the central Andean subduction zone. Regions above 3000 m are dark grey, indicating the approximate extent of the Central Andean Plateau. Contour lines show the depth of the Wadati–Benioff–Zone (Cahill and Isacks, 1992). White triangles indicate active volcanoes. Well located earthquakes of the last 30 years (Engdahl et al., 1998) are plotted for the mantle as circles (depth > 40 km) and the crust as crosses (depth < 40 km). Crustal seismicity is confined to the seismogenic part of the subduction zone and the foreland thrust belts. The study area and extent of Fig. 2 is outlined by the rectangle. The highly symmetrical Central Andean Plateau lies above a region of moderately steep (30°) subduction and is flanked by regions of flat subduction.

The Western Cordillera, Altiplano, and Puna are extensively covered by late Miocene to recent crystal-rich ashflow deposits. Ignimbrite volcanism has been attributed to melting of thickened crust (de Silva, 1989). Further magmatism in the backarc is restricted to mafic monogenetic cones and fissure flows. Based on trace-element characteristics, Kay et al. (1994, 1999) distinguished three volcanic groups. An intra-plate group occurs above the current seismic gap in the southern Puna (26°S–27°S, Cerro Galàn). Intermediate volume calc–alkaline lavas are found just to the north, south, and west of the intra-plate flows. Further to the north, at 24°S, small shoshonitic flows occur locally along the El Toro fault zone. The change from shoshonitic chemistry to calc–alkaline to intra-plate-type basalts from north to south is regarded as evidence for lithospheric thinning. Based on the particular chemistry of these mafic magmas, geophysical data (Whitman et al., 1992), and because there is no horizontal crustal extension, lithospheric detachment has been postulated to have occurred beneath the southern Puna (Kay and Kay, 1993).

Cerro Tuzgle in the easternmost Puna is the only Quaternary backarc strato-volcano. Its magmas formed

by a complex mixing process in the mantle and thickened crust (Coira and Kay, 1993). The Tuzgle volcanic rocks can be divided into two groups with different mantle precursors: an older, more voluminous rhyodacitic to mafic andesitic sequence and a younger andesitic one (Coira and Kay, 1993). Cerro Tuzgle is situated directly above a vigorous earthquake cluster at a depth of about 200 km (Figs. 2 and 3).

2.1. Data

The SFB 267 "Deformation Processes in the Andes", carried out four passive seismic experiments between 1994 and 1997, deploying portable, mostly short-period, seismograph arrays between 20°S and 25°S from the Pacific coast across the Andean mountain range. In this study, data from three of these experiments are used. The PISCO'94 (Graeber and Asch, 1999) deployment covered the eastern forearc and the volcanic arc of Chile between 22°S and 24°S (Fig. 2). The passive part of the ANCORP'96 experiment (ANCORP Working Group, 1999) extended PISCO coverage to 20°S in the north and additionally placed eight seismographs on the backarc of the Bolivian Altiplano; unfortunately, due to logistical difficulties and bad weather, few data could be recovered from these stations. Additionally, travel times from a deployment of the Universidád de Chile near Iquique are included. The PUNA'97 array (Schurr et al., 1999) was centered on the Puna plateau in the Argentine backarc region. The forearc and Chilean arc were also covered by stations on former PISCO sites and seven single-component seismographs operated by Universidád de Chile (Fig. 2). All three experiments were very similar in instrumentation and set-up. Most sites were equipped with PDAS data loggers and MARK L4-3d short-period (1 Hz) three component seismometers. The seismographs' internal clocks were synchronized to universal standard time using the Global Positioning System; accuracy should be within 10 ms. Most stations recorded continuously at 100 samples per second. Each of the three networks recorded for about three months. Average station spacing was about 40 km.

Fig. 3 shows locations of the earthquakes used in the travel time tomography. Only events lying within

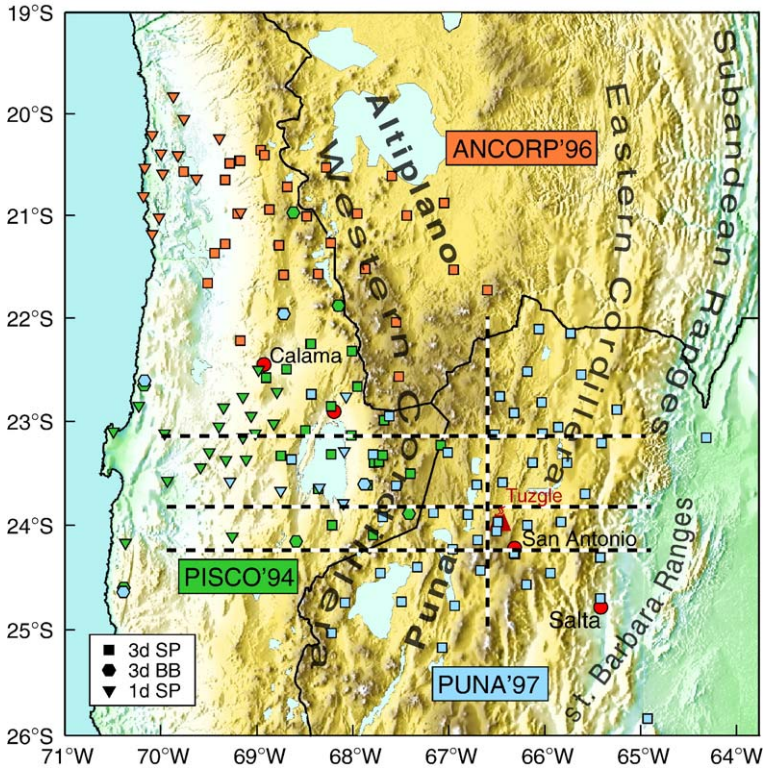

Fig. 2. Topographic map of the station arrays used in this study. The different symbols mark seismograph locations and are coded after seismograph type (legend: SP = short-period, BB = broad-band) and deployment (colour). Inverted triangles (1D seismographs) are networks operated by Universidad de Chile. Dashed lines indicate the locations of cross-sections in Fig. 10. Major morpho-tectonic units and location of Cerro Tuzgle are marked.

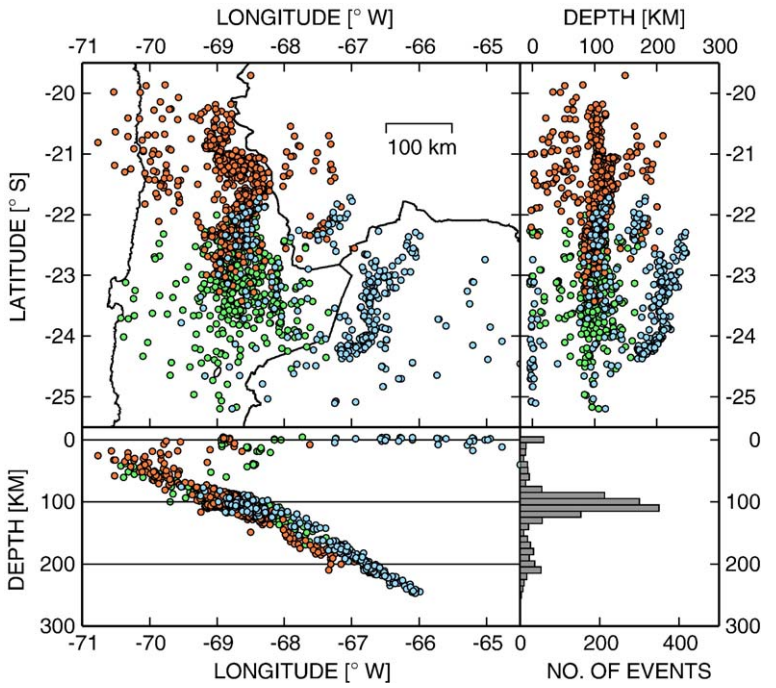

Fig. 3. Epicenter map, E–W and N–S hypocenter projections of events used in this tomographic study. Colour scheme is the same as in Fig. 2 for the three data sets. Most events are of intermediate depth and occur between 100 km and 250 km depth.

the footprint of the network (i.e. gap < 180°) were selected. Earthquake epicenters overlap where the three networks join, improving resolution especially in those regions of the model that were critical for the individual data sets. Most events are of intermediate depth (100–250 km), originating in the Wadati Benioff Zone of the subducted Nazca plate. Crustal events are rare, weak and mostly very shallow. Events in the Benioff Zone are not evenly distributed, but occur in several elongated clusters at different depth levels (Fig. 3). Distribution of earthquake hypocenters is crucial for the screening of the model volume, and thus for the spatial resolution capability of the data set. Lack of events shallower than 80 km hampers resolution at crustal depths, this is especially true for the eastern part of the model.

Data used in this study are *P* and *S*–*P* travel-times, and *t** parameters calculated by inversion of *P*-wave spectra (Rietbrock, 2001). All travel times were handpicked and weighted based on the estimated uncertainty. These weights were used later in the inversion procedure. *P* picks, due to their impulsive onset, could often be determined within a few samples accuracy. *S* picks were made on rotated and integrated records to avoid compressional wave precursor and enhance the low frequency signal. *S* arrival times at stations in the Western Cordillera and on the Puna plateau are few and often inaccurate due to the very strong attenuation (Fig. 4).

*t** operators were determined from smoothed (Park et al., 1987) amplitude spectra of 2.56-s time windows following the *P* arrival (Fig. 4). In the non-linear inversion scheme, a Brune-type ω^2 source model and frequency-independent attenuation is assumed. Whole path attenuation (*t**) and signal moment (spectral plateau) are determined for each ray, and a corner frequency is determined for each source. This accounts for variable attenuation structure and radiation from the source. Source directivity is neglected, which appears justified for the small magnitude events used (M_l 1.0–5.0). For each signal spectrum, a noise spectrum was also determined from a time window preceding the *P* wave. A signal to noise ratio of three in a continuous portion of the spectrum was required for *t** to enter the Q_p inversion. The high spectral decay and low signal energy of *S* waves at many stations prohibited a comprehensive Q_s analysis. The combined data set comprises 33,018 *P* arrival-times, 17,123 *S* arrival times and 20,145 *t** values from 1558 events (571 from PISCO, 669 from ANCORP, and 318 from PUNA) recorded at more than 150 stations.

Three-component seismograms and *P*-wave spectra, as well as a map displaying whole path Q_p for one event recorded at the PUNA array are shown in Fig. 4. Most

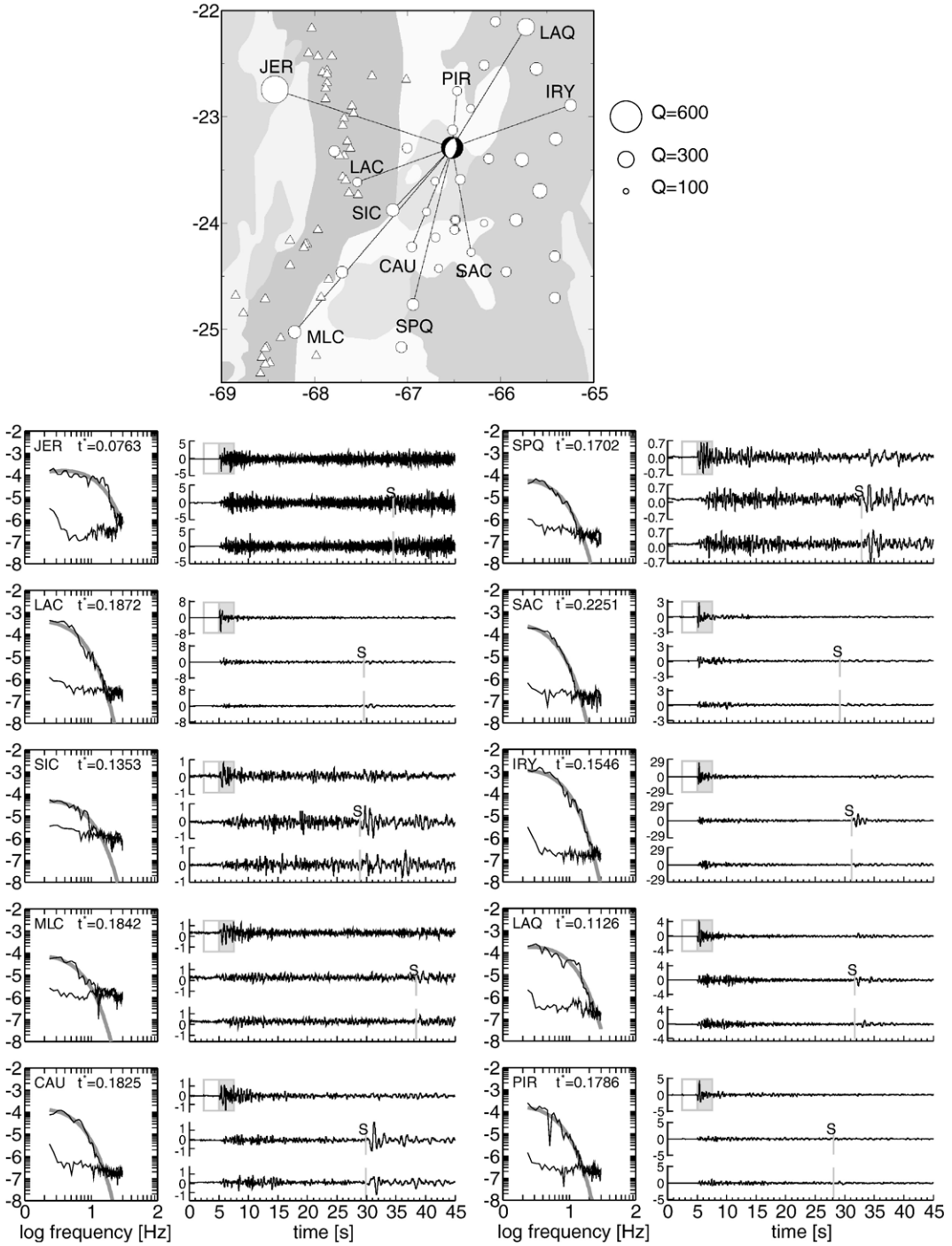

Fig. 4. Velocity seismograms and *P*-wave spectra for an intermediate depth event recorded at the Puna network. Vertical (upper trace) and horizontal component seismograms are shown for the paths marked on the map. For the 2.56 second windows before and after the *P* arrival, noise and signal spectra, as well as the modeled spectra (thick grey line) are shown. On the map, the size of the white circles is scaled after whole-path-*Q* calculated from the *t** parameter and travel time. Grey shades distinguish major geomorphological units while triangles depict volcanoes. Q_p is high for paths to the west (forearc) and east (Eastern Cordillera), and low for stations in the Puna.

seismograms are simple with impulsive direct arrivals and little coda. Only paths in and along the slab into the forearc (e.g. station JER) show strong coda and much higher frequency content (and also high Q_p). Strong attenuation is visible in the raw short-period seismograms at many stations (note different amplitude scales in Fig. 4). For some paths, this leads to a complete lack of *S* energy. Attenuation is also seen in the shape of the *P* wave spectra, where it is exploited to determine the t^* operator.

2.2. Tomography

We use the computer code *simulps* (Evans et al., 1994) for simultaneous inversion of 3D structure and hypocentral parameters. It was originally developed by Thurber (1983), but experienced many modifications subsequently (e.g., Um and Thurber, 1987; Eberhart-Phillips, 1993; Rietbrock, 1996; Thurber and Eberhart-Phillips, 1999). The structural model is defined on nodes at the intersections of a possibly unevenly spaced rectangular grid, and model parameters between neighbouring grid nodes are determined by linear B-spline interpolation. Parameter separation (Pavlis and Booker, 1980) is applied for the coupled hypocenter-velocity problem. The damped least squares solution of the model equations is resolved by Cholesky Decomposition. Ray tracing is done by a two-step procedure using approximate ray tracing and pseudo-bending (ART/PB) (Um and Thurber, 1987).

ART/PB is not exact, and it has been pointed out that especially for long rays (>80 km) caution is appropriate (Prothero et al., 1988). Haslinger and Kissling (2001) and Husen and Kissling (2001) tested a 3D shooting and finite difference ray tracer on synthetic and real data against ART/PB. For their test cases, errors in ray path and travel time were small (<10 ms), and effects on the inversion result were small. We accounted for the long rays specific to the subduction zone environment of this study by making two changes to the ART/PB algorithm to obtain more accurate travel times. First, we force the ray to have no curvature for path segments for which PB does not succeed. This is always the case, when there are sections of constant velocity. Thus rays are straight, instead of arcuate, in constant velocity regions. Second, we bisect the initial ray found by ART. For the two segments both ART and PB is performed again, refining the initial ray. Additionally, the number of segments constituting each ray is raised compared to the original code. This is important because time errors for the long rays result mainly from the constant curvature arcs initially used in ART. This is not appropriate for the Benioff Zone events, for which rays first travel through the slab or in the mantle with small velocity gradients before they penetrate the crust.

We tested our modified algorithm against the original ART/PB and a finite difference (FD) algorithm (Podvin and Lecomte, 1991). Rays and travel times were calculated for both a synthetic model (slab, mantle wedge, and crust with constant velocities) and our final model (Schurr, 2001). In both these cases travel times from the modified ART/PB are much improved compared to the original one with the FD times as reference. The largest differences arise for rays that travel long distances in the mantle or slab. Differences to the FD times rarely exceed 0.1 s. This is in the order of picking accuracy, and less than 0.5% of the total travel time for longer rays, and should not affect the inversion results.

The inversion grid determines the maximum spatial resolution of the model. We use a horizontal spacing in the east–west direction of 25 km in the forearc and arc, where ray coverage is densest, and 30–40 km in the backarc. In the north–south direction, parallel to the strike of the mountain range, nodes are 40 km apart. At depth, spacing is 20 km in the crust and 25 km in the mantle. This is fine enough to resolve major tectonic structures and assures well resolved nodes over most parts of the model.

Objective, simple starting models are important to avoid artefacts in the inversion results introduced by a priori information (Kissling et al., 1994). A commonly followed procedure is the derivation of a 1D model from the same travel time data that is later used in the 3D inversion ("minimum-1D" model (Kissling et al., 1994)). We followed a slightly modified approach. The dominant structural anomaly influencing arrival times for the Benioff Zone events is the fast subducted Nazca lithosphere. Because the longest rays in the mantle travel along the fast Nazca plate to the western network stations, 1D velocities in the mantle are biased towards the anomalous high velocities of the slab, and as such represent rather the anomaly than the background mantle. Because there is a trade-off between earthquake depths and average velocities for our data set, such biases are not completely removed in the 3D inversion.

To account for these problems we parameterize the starting model into an upper and lower crust, mantle wedge, and subducted slab. This is done in practice by tying inversion nodes of a 2D grid together (Thurber and Eberhart-Phillips, 1999). Crustal nodes start with 6.0 km/s at 20 km depth, and 6.5 km/s at 40 km depth in accordance with seismic data from Wigger et al. (1994). At 60 km depth, nodes have a velocity of

Table 1
Starting model for v_p

Depth (km)	v_p (km/s)
20	5.98
40	6.51
60	7.41
>85	8.20

7.5 km/s to represent a gradual transition to mantle values. Starting mantle velocities are borrowed from the IASPEI model (Kennett, 1991). We then use the inverted crustal and mantle wedge velocities as a 1D starting model that is not biased by the subducted slab (Table 1).

For v_p/v_s, and Q_p we started the 3D inversion from a homogeneous half space ($v_p/v_s = 1.75$, $Q_p = 600$). These numbers best fit the data in a suite of inversions with different values. In the inversion of v_p/v_s, v_p was strongly overdamped. For Q_p the 3D v_p model was used for ray tracing and hypocenters were constant during the inversion. Damping is important to stabilize the inversion and smooth the model. Because damping balances between solution length and data fit, an objective choice can be made from a trade-off-curve, graphing model-variance versus data-variance for different damping values (Eberhart-Phillips, 1986). For all three inversion parameters, we have chosen a conservative value that is close to the minimum data-variance, yet yields only a moderate model-variance.

The results of the tomographic inversion are shown in Figs. 5 and 6. The 3D models strongly reduce travel time (t^*) residuals (Fig. 7). For the final models, the previously broadly distributed and skewed residuals cluster symmetrically around zero, indicating successful inversions. The variance of the travel time (t^*) residuals is decreased by 77% for v_p, by 60% for v_p/v_s, and by 85% for Q_p.

2.3. Resolution

To gauge resolution and errors we exploit the model resolution matrix and invert a synthetic data set with a ray geometry identical to the real one. We plot both the size of the diagonal elements (DE) of the resolution matrix (RM), and the spread value (Menke, 1989; Michelini and McEvilly, 1991) that is calculated from an entire row of the RM (averaging vector). The spread value incorporates two aspects of resolution: the size of the averaging vector and its peakedness. A perfectly resolved model parameter has a zero spread value, whereas large values correspond to broad shapes of the averaging vector. For poorly resolved nodes, the averaging vector is contoured to display the direction of smearing (Eberhart-Phillips and Michael, 1998).

Fig. 8 shows spread values (grey shades) and DEs (white circles) for the three inverted attributes. 70% contours of the averaging vector are drawn for those nodes for which off-diagonal elements reach 70% of the DE. Absolute values of spread and DE's strongly depend on damping, thus only their relative size is interpreted. For velocities and Q_p, resolution is best in the forearc above the clustered earthquakes at 100 km depth, where ray coverage is densest. Vertical smearing occurs mainly in the uppermost layers. Q_p and v_p/v_s lack data from the western vertical short-period instruments operated by the Universidad de Chile, causing diminished resolution there. North of 22.8°S, resolution in the backarc (east of 68°W, Altiplano) is low, and significant smearing is indicated by small spread values and averaging contours. South of 22.8°S, where the backarc is covered by the PUNA network, resolution is quite evenly distributed and good to fair everywhere but the margins of the model. Smearing is mostly vertical and occurs for the shallow and easternmost nodes. Smearing is more severe for Q_p and v_p/v_s, because important subhorizontal rays from earthquakes in the forearc are fewer due to strong attenuation and low signal to noise ratios. Here anomalies may be recovered, but their geometry is probably blurred. For each attribute a threshold for the spread value has been chosen to separate high and low resolution. The choice is based on the relative size of the spread and on synthetic experiments. These spread contours are marked by the thick black lines in Fig. 8, and are also drawn into the tomographic models in Figs. 5 and 6. As their choice is somewhat arbitrary, they should be considered with due caution.

Tests with synthetic data have been conducted to reveal inherent limitations in resolution and possible artefacts due to event-station geometry and chosen parameterization. We trace the same rays as in the respective real data set through a synthetic model to calculate travel times and t^* operators. Realistic, normally distributed, random noise, scaled to the individual estimated pick uncertainty for the travel

Fig. 5. West–east depth sections through the 3D Q_p, v_p, v_p/v_s models. For v_p deviations from the 1D background model (Table 1) are displayed. Latitude of the sections is indicated in the lower left corner. Earthquakes, stations, and volcanoes within 20 km of the section are also plotted. The thick, white contour line encloses regions of good resolution defined by the spread value. Regions of poor resolution are displayed in slightly faded colour.

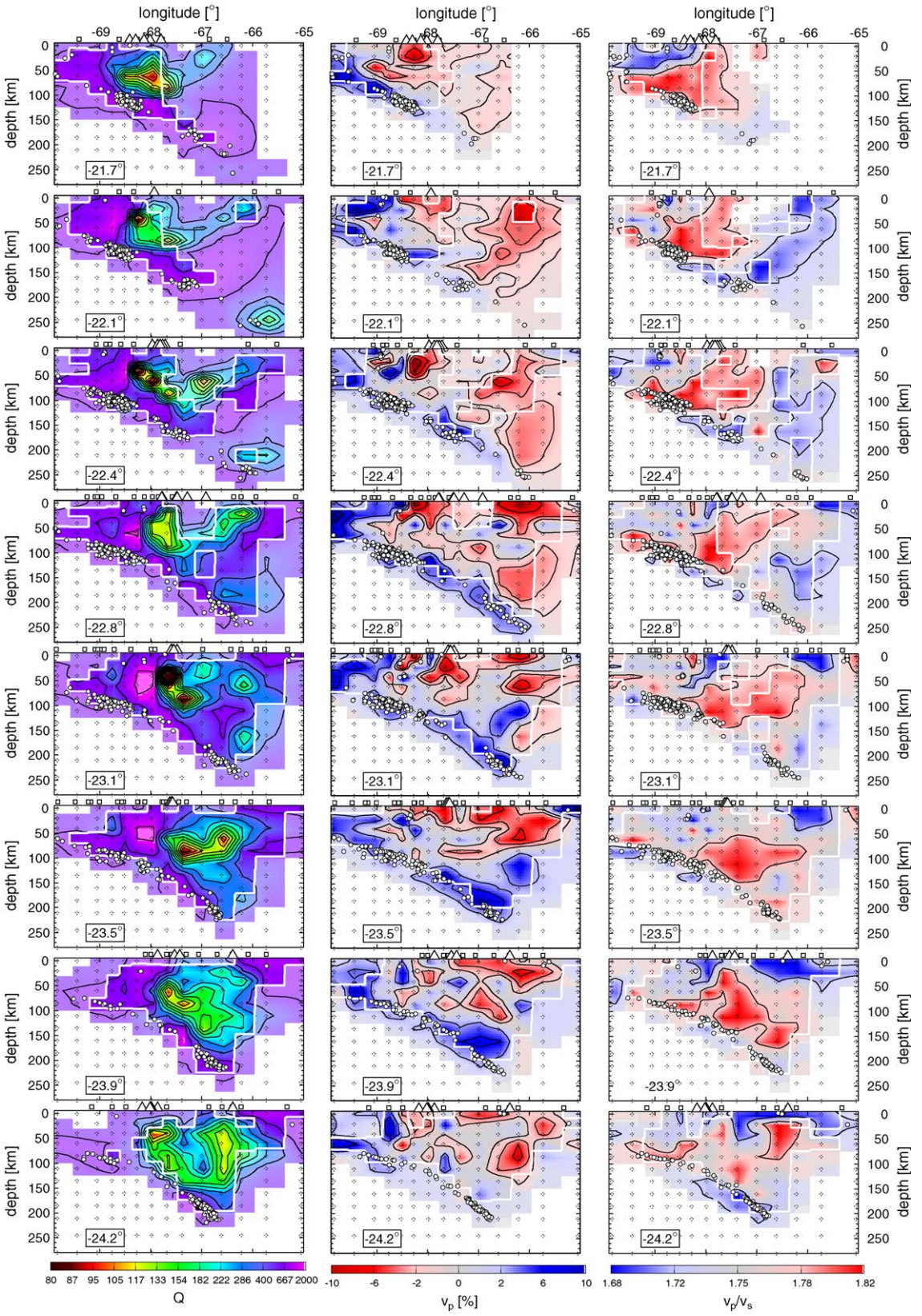
longitude [°]
-69
-68
-67
-66
-65
depth [km]
0
50
100
150
200
250
-21.7°
-22.1°
-22.4°
-22.8°
-23.1°
-23.5°
-23.9°
-24.2°
80 87 95 105 117 133 154 182 222 286 400 667 2000
Q
-10 -6 -2 0 2 6 10
v_p [%]
1.68 1.72 1.75 1.78 1.82
v_p/v_s

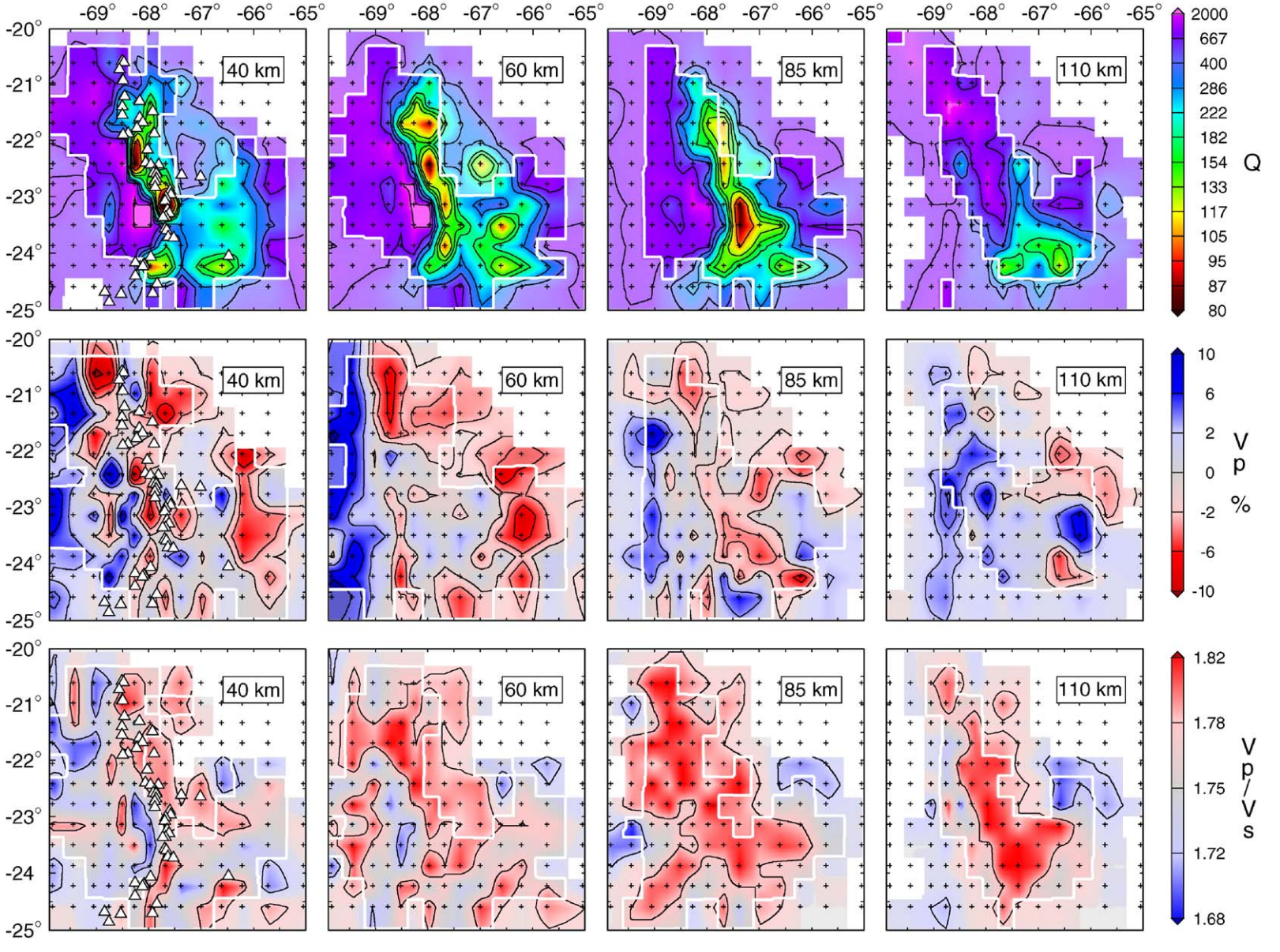

Fig. 6. Depth maps of Q_p, v_p, v_p/v_s. Depth is indicated in the upper right corner. The thick white contour encloses regions of good resolution defined by the spread value. Regions of poor resolution are displayed in slightly faded colour.

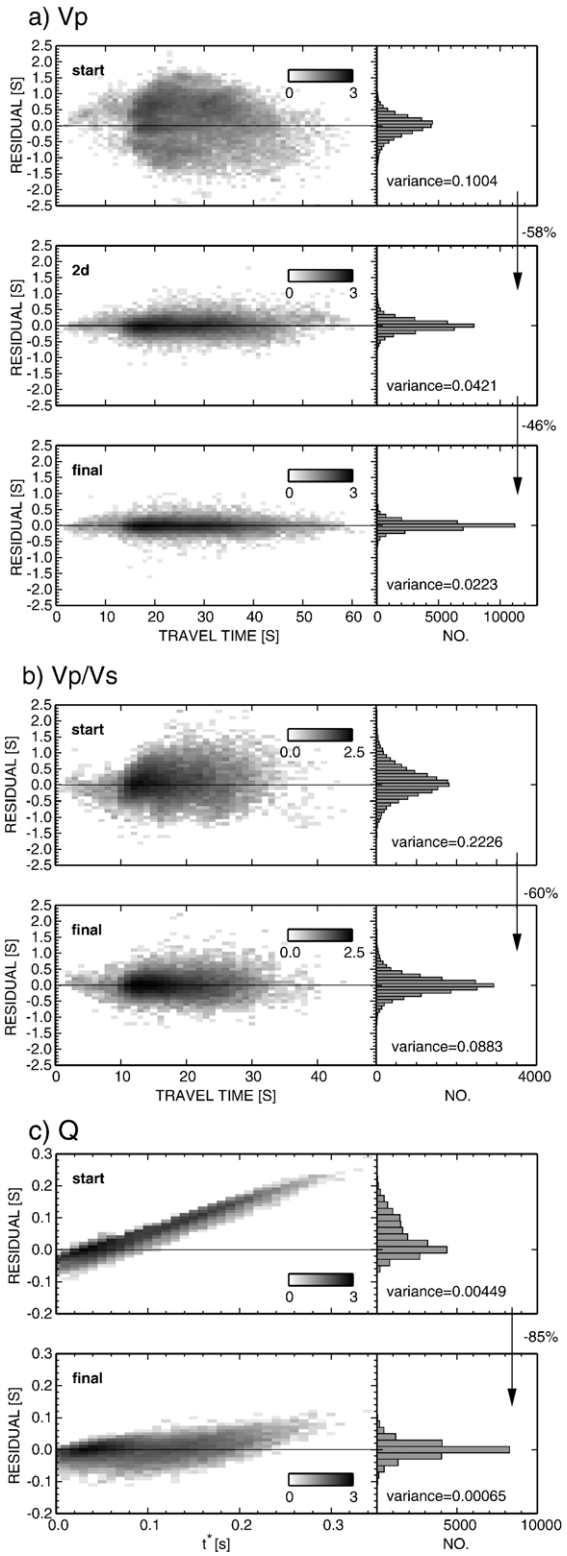

Fig. 7. Travel time and t^* residuals are graphed against travel times and plotted as densities (logarithmic grey scale) before and after the inversions for (a) v_p, (b) v_p/v_s, and (c) Q_p. Residual histograms are also shown. After the 3-D inversions, residuals cluster symmetrically around zero, and data variances are drastically reduced.

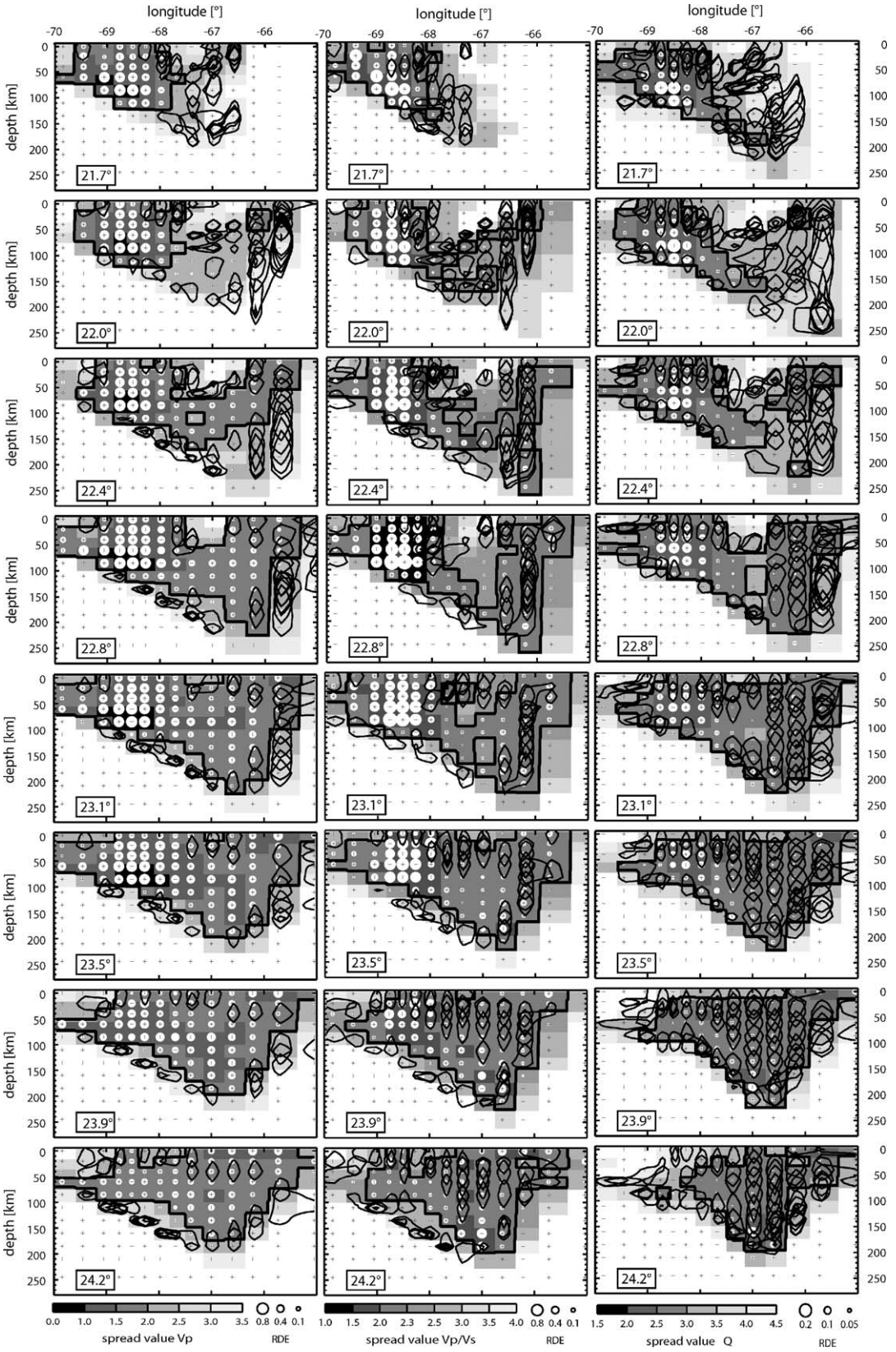
longitude [°]
-70 -69 -68 -67 -66
depth [km]
0 50 100 150 200 250
21.7°
22.0°
22.4°
22.8°
23.1°
23.5°
23.9°
24.2°
0.0 1.0 1.5 2.0 2.5 3.0 3.5 0.8 0.4 0.1
spread value Vp
RDE
1.0 1.5 2.0 2.3 2.5 3.0 3.5 4.0 0.8 0.4 0.1
spread value Vp/Vs
RDE
1.5 2.0 2.5 3.0 3.5 4.0 4.5 0.2 0.1 0.05
spread value Q
RDE

times, and with a constant standard deviation of 0.008 s for t^* is added to the synthetic data.

We choose a simple checker board with alternating high and low anomalies as input. For v_p the 1D input starting model is perturbed with 5% anomalies, for v_p/v_s, alternating anomalies with 1.66 and 1.85, and for Q_p with 300 and 1500 replace the homogeneous starting model. The simple checker board pattern gives a good overview of resolving power for the multiple sections and attributes. For other more realistic input models see Schurr (2001) and Schurr et al. (2003). The synthetic data sets have been inverted applying the same procedure as for the real data. The inverted models are shown in Fig. 9.

For all three attributes, structures in the forearc are recovered best. Here seismicity is highest and data quality is not hampered by attenuation. Amplitudes are only slightly underestimated. The WC is only well resolved between 22.5°S and 24.5°S where both its western and eastern flanks were covered with stations. North of 22.5°S only the western part of the WC is recovered reliably. Resolution of v_p/v_s is severely diminished and particularly shallow structures are not resolved. This is due to the lack of *S*-wave data caused by strong attenuation. Q_p resolution is generally good in the WC. Resolution in the backarc varies: In the north, in Bolivia, where parts of the southern Altiplano were covered during the ANCORP deployment, resolution is poor due to few data for all three attributes. Here, severe smearing is observed. Further south, beneath the footprint of the PUNA network, resolution is good for v_p and Q_p. Anomalies are well recovered with only slightly underestimated amplitudes and little smearing in the slab region and the mantle wedge. Particularly for Q_p, shallow structures are not well recovered. Smearing occurs for the easternmost columns of nodes. For v_p/v_s, the amplitudes of the anomalies are strongly underestimated and smearing occurs.

In general v_p delivers the sharpest image of the structures for the three data sets. For Q_p, the amplitudes of the positive anomalies are underestimated. In the mantle wedge, structures are recovered in the central part. In the east and north-east of the model, severe smearing along the ray paths occurs. Magnitude of errors up to 0.3 km/s for v_p, over 500 for high Q_p regions, and up to 0.03 for v_p/v_s, can also be expected for the real data set. Note, however, that amplitudes of inverted anomalies are strongly influenced by the damping parameter chosen for the inversion. It can be expected that the inversions of the real data sets are affected by similar smearing effects. Regions of good resolution defined by the spread value are generally confirmed by the synthetic tests.

3. Results

Results are presented on E–W cross-sections and depth maps (Figs. 5 and 6). Sections that are crucial in for the interpretation between 23.1°S and 24.2°S along with a N–S slice along 66.6°W are displayed enlarged in Fig. 10. The spread contour line enclosing regions of good resolution, defined above, is superimposed, and the outside region of lower resolution appears in slightly faded color. v_p is represented as deviation of the 1D starting model (Table 1). In this representation, subtraction of lithological and pressure-induced 1D background, reveals patterns that are depth independent and cross lithological contacts (i.e. Moho). Thus effects from variations in the state of the rocks, like temperature or the presence of water, are more easily seen, and comparison with the other two attributes is facilitated.

Because v_p/v_s and Q_p inversions start from a homogeneous half-space, and their values are not, to a first degree, pressure dependent, absolute values are plotted. We prefer to discuss attenuation in terms of Q_p instead of Q_p^{-1}, which is actually inverted for Q_p is commonly used in the literature and absolute numbers are more familiar than their reciprocal. Actual sensitivity of the data to Q_p^{-1} is accounted for by the non linear colour scale, that is equidistant in Q_p^{-1}, giving much higher dynamic range for low Q_p than for higher Q_p.

The seismic attributes reveal a heterogeneous crust and upper mantle system with sharp gradients and strong anomalies. Results are presented for the major tectonic units: forearc, Western Cordillera, slab, and the backarc plateau, with an emphasis on the latter.

3.1. Forearc

v_p tomography reveals a relatively fast forearc crust (6.5 km/s upper crust, 7 km/s lower crust), and reduced velocities (7.5 km/s–8 km/s) in the thin mantle wedge west of approximately 68°W. The forearc crust is characterized by normal v_p/v_s values (approximately

Fig. 8. Spread values (grey shades) and resolution diagonal elements (RDE, white discs) for the v_p, v_p/v_s, Q_p inversion nodes for the same latitudinal cross sections as in Fig. 5. Dark shades and large discs indicate good resolution. Superimposed are 70% contour lines of the averaging vector to visualize spatial smearing (see text for further explanation). Contour lines are only drawn for nodes where off-diagonal elements reach 70% of the RDE.

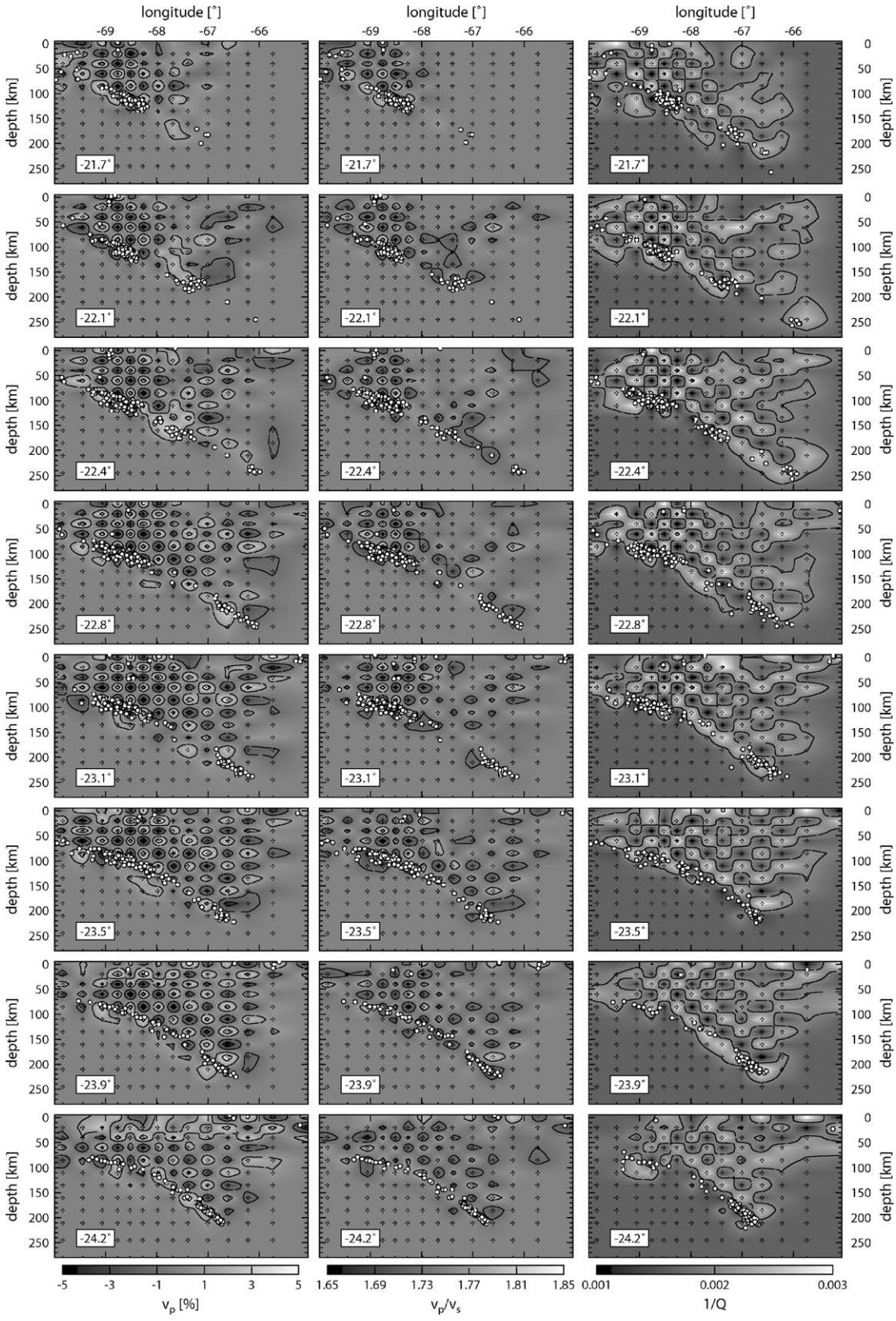

Fig. 9. Reconstruction of synthetic checkerboard models for v_p, v_p/v_s and Q_p for the same cross sections as in Fig. 5.

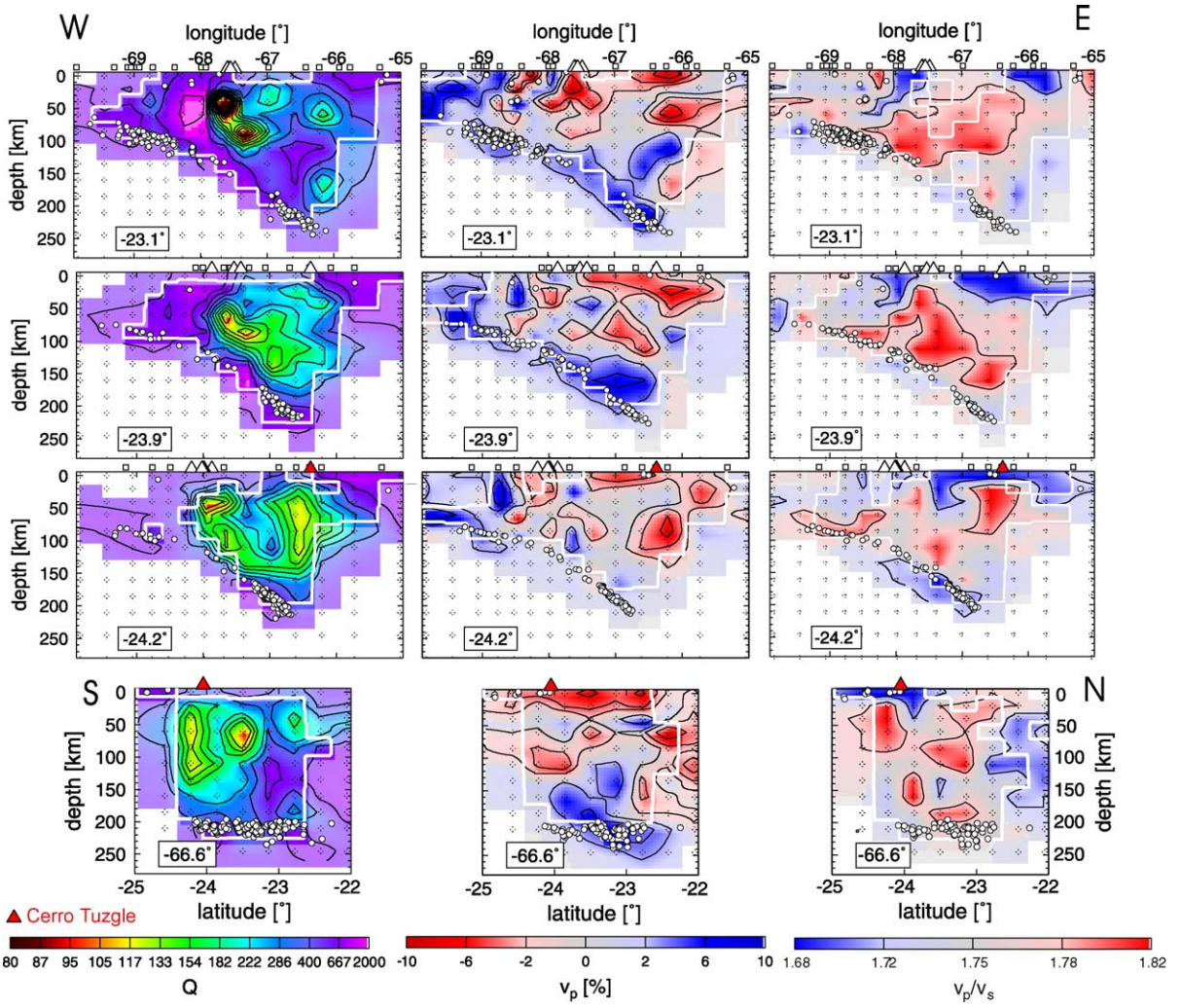

Fig. 10. Detail of three cross sections (west–east) for v_p, v_p/v_s and Q_p out of Fig. 5 as well as a perpendicular slice (north–south). See Fig. 2 for location of sections. Note the high v_p and Q_p regions dipping against the slab into the backarc mantle, and the low v_p and Q_p regions engulfing it. In the south, there is a region of low v_p and Q_p beneath the backarc volcano Cerro Tuzgle.

1.73–1.78). The mantle wedge has clearly elevated v_p/v_s ratios (>1.8; see 85 km depth map in Fig. 6). Q_p shows a rather undifferentiated forearc with continuously high Q_p (600–2000). There are no perceptible differences between crust and mantle. The transition to the WC is very sharp and occurs essentially from one inversion node to the next (Figs. 5 and 6).

3.2. Western Cordillera

A crustal low velocity, low Q_p, and elevated v_p/v_s zone closely follows the belt of active volcanoes forming the current magmatic arc (Fig. 6). Q_p appears to be affected most strongly by the volcanic processes. The crustal Q_p anomaly is most pronounced in the center of the study area, and dies out to the north and south. Q_p is everywhere below 200, with isolated pockets of 80 and less. The Q_p anomaly correlates with a continuous low v_p zone. v_p is lowest in the upper 20 km (first two rows of nodes). Strongest Q_p anomalies are at 40 km depth, but probably reach the surface, based on the large station corrections. Stronger damping of the station corrections in the inversion places strong Q_p anomalies in the uppermost layers beneath the discrete station locations. The eastern boundary of the magmatic arc is not well defined on the tomographic maps, and low velocities and Q_p reach well into the backarc crust. The strong crustal Q_p anomalies are always connected to the mantle wedge. In the sections north of 22.5°S, low Q_p zones appear to originate directly above the earthquake clusters at 100 km depth. To the south, where the magmatic arc is displaced eastward, mantle anomalies

lose connection to these clusters and reach deeper and eastwards to the seismicity at 200 km depth. The high v_p/v_s anomaly described for the forearc also reaches well beneath the magmatic arc. Strongest anomalies are found in the mantle wedge and lower crust. Diminished resolution for v_p/v_s in the shallow crust beneath the Western Cordillera may be responsible for a lack of shallow anomalies.

3.3. Slab

The subducted oceanic Nazca lithosphere is imaged as a continuous, fast, high Q_p body dipping eastwards, and enveloping the Wadati Benioff Zone. Velocities are fastest around 23°S near the earthquake cluster at 200 km depth. There, velocities of 8.7 km/s are reached but may be overestimated according to the synthetic tests. Q_p in the slab is around 1000, but might be underestimated according to the synthetic tests. v_p/v_s is slightly reduced. Between 23.5°S and 24°S and 150 km and 200 km depth, the slab thickens considerably, and a zone of high velocity material sits above the sharply defined Benioff Zone. This section is well resolved and synthetic testing does not suggest any artefacts.

3.4. Backarc

The backarc crust is characterized by generally reduced crustal velocities (6 km/s–6.5 km/s) and low Q_p (200–300) with isolated stronger anomalies (Fig. 10). v_p/v_s is close to normal for felsic rocks (~1.7) in the uppermost crust (first 20 km). At this depth, additional constraint in some areas (around and south of 24°S) comes from shallow crustal earthquakes. Increased v_p/v_s values are found in the lower crust with a strong anomaly around 24°S, beneath the active backarc volcano Tuzgle. This anomaly extends into the upper mantle and coincides with low Q_p and low v_p. *P* velocities are extremely low in the upper crust beneath the north-western part of the PUNA network. There, Q_p is also reduced and large station corrections indicate a strong anomaly at shallow depth. Receiver functions show strong negative conversions indicating a LVZ at 20 km depth at these stations (Yuan et al., 2000). In the lower crust, low v_p and Q_p values are also found beneath the Puna and bordering Eastern Cordillera around 66.5°W in the sections at 23.1°S and 23.5°S. These anomalies extend into the upper mantle and have similar geometries for both parameters. A prominent high-velocity, high-Q_p body, clearly seen in the same sections, dips from the uppermost mantle westward down to the slab at ~150 km depth. The body is well resolved (Figs. 8 and 9). Both velocity and Q_p for this anomaly are similar to values found in the subducted slab. All around this high v_p and high Q_p, regions of low velocity and Q_p zone are observed (Fig. 10). There is a pronounced separation in the mantle wedge attenuation structure at around 23°S (see the 110 km depth map in Fig. 6), where to the north, mantle Q_p values are normal to high, and to the south, they are low.

4. Discussion

The tomographic images of the Andean subduction system and its related volcanic and orogenic belts reveal a consistent but complex lithosphere–asthenosphere system that is controlled by both, tectonic (e.g. lithospheric shortening) and specific subduction-related (e.g. dehydration of the slab and melting in the mantle wedge) processes. On a large scale, elastic and anelastic properties correlate quite well with expectations from simple thermal models of subduction zones (e.g., Peacock, 1996), suggesting that homologous temperature is the governing factor for the observed first order patterns.

Oceanic lithosphere that has been cooled and thickened since the time of its formation (Parsons and Sclater, 1977) is subducted with a surface temperature of approximately 0 °C at rates much faster than thermal diffusion times. Accordingly, it is much cooler than the ambient mantle during most or all of its descent. This temperature difference can be seen as a 6% to 10% positive v_p anomaly that engulfs the Wadati Benioff Zone to a depth of 250 km, where resolution fades. The amplitude of the anomaly corresponds quite well with a thermal contrast of 600–800 °C (Sobolev et al., 1996), as it is expected between a 400–600 °C cold slab and a 1000–1200 °C hot mantle wedge (see for example the thermal model in Peacock (1996) for a 50 Ma old slab subducted at 10 cm/year, a situation comparable to the Andes). The low temperatures also cause the low attenuation that is measured for the slab (Q_p = 1000–2000).

Due to continuous subduction of cold oceanic lithosphere, forearcs are also cold. This is manifested, for example, in surface heat flow values that are among the lowest on earth (Springer and Förster, 1998). The low temperature forearc is best exemplified by the high Q_p values obtained trench-ward of the volcanic front. Intrinsic Q_p is a particularly good gauge for temperature, because it is less sensitive to lithology than v_p and v_p/v_s. The generally high *P* velocities that

also characterize the forearc, might indicate a mafic lithology due to its history of migrating volcanic arcs, although temperature might play an additional role. The mantle wedge beneath the forearc has very high v_p/v_s values (>1.8; see the 85 km layer in Fig. 6). These high values have already been noticed by Graeber and Asch (1999) and were interpreted as serpentinites that are produced by hydration of peridotite at relatively low temperatures and pressures.

In the easternmost part of the model, between 65°W and 66°W, the crust, where it is resolved, again shows low attenuation. This, together with relatively low values for v_p/v_s, might indicate the cold, felsic foreland crust that forms the backstop for the Andean orogeny.

Between the seismically strong forearc and foreland, the Andean arc and Puna high plateau is characterized by low Q_p, low v_p, and high v_p/v_s values in crust and mantle. These seismic properties are certainly an expression of subduction-related magmatism (Schurr et al., 2003) and crustal shortening that is exemplified at the surface by an active volcanic arc, high heat flow, widespread felsic and mafic volcanism in the backarc, as well as plateau formation. The seismic properties of the Puna mantle point to dominantly asthenospheric conditions. This is in contrast to the apparently intact mantle lithosphere found beneath the northerly Altiplano (Whitman et al., 1992; Myers et al., 1998; Haberland et al., 2003).

In the following sections, we focus in more detail on the backarc part of the model. For detailed discussions of the forearc, see Schurr and Rietbrock (2004), and for the arc and subduction-related processes, Haberland and Rietbrock (2001) and Schurr et al. (2003).

4.1. Lithospheric detachment beneath the northern Puna

The concept of lithospheric detachment has been introduced to explain the absence of a thick mantle lid beneath elevated plateaus (Bird, 1979; Houseman et al., 1981) and rapid uplift and mafic magmatism often accompanying the late stage of the orogenic process (Kay and Kay, 1993). In this model, thickened, cold lithosphere becomes gravitationally unstable, detaches from the lower crust, and sinks into the underlying mantle. The missing lithosphere is replaced by an influx of hot asthenosphere causing uplift of the crust and volcanism. Although lithospheric detachment has been proposed in many locations (the Himalayas, Andes, Alps, the Basin and Range province of the Western United States, the European Variscides), geophysical observations of the process are very few (Kosarev et al., 1999; Boyd et al., 2004). This may be due to its ephemeral nature: numerical modeling indicates that lithospheric detachment is a catastrophic event that lasts only a few million years (Houseman et al., 1981; Schott and Schmeling, 1998).

Near 23°S in the northern Puna of the central Andes, we image a fast, high Q_p body that dips westward from the base of the easternmost Puna crust 100 km down to the subducted Nazca plate (Fig. 10). South of this body the mantle wedge has low velocity and Q, and the Nazca plate thickens by several tens of kilometres above the sharply defined Benioff Zone. This region of mantle wedge and slab is well resolved. Anomalies in velocity and attenuation have to a first degree the same physical cause: variations in homologous temperature (Berckhemer et al., 1982; Jackson et al., 1992). Because velocity and Q_p images are based on independent measurements

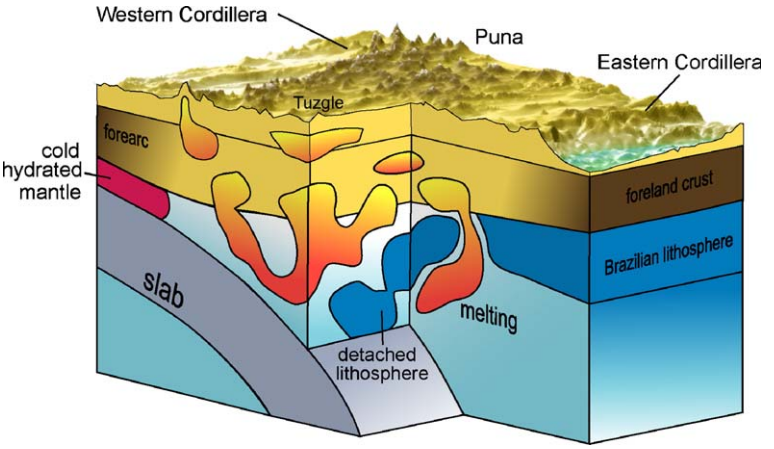

Fig. 11. Interpretational model based on the tomographic results. See text for explanation.

(travel times and spectral shapes), their congruence gives additional confidence in the results. The fast, high-Q_p region appears sharper in the velocity image. This may be caused by the non-linear resolution of Q_p, making variations in high-Q_p regions more difficult to resolve than variations for low Q_p. Above the high-v_p, high-Q_p region in the mantle, high attenuation and low velocities are found in the uppermost mantle and lower crust. Adjacent highs and lows in tomographic models have to be considered carefully because they could be an artefact. We verified that the structures in crust and mantle are decoupled by inverting only for mantle structure while fixing a homogeneous crustal structure and vice versa. Both, the anomalies, in the mantle wedge and in the crust, could this way be imaged independently.

We interpret the imaged fast, high-Q_p body as detaching lithosphere that has been shortened and thickened beneath the Eastern Cordillera and parts of the Puna plateau (Fig. 11). The cold, sub-crustal mantle sinks much faster than thermal diffusion times into the underlying hotter asthenosphere, causing the strong velocity and Q_p contrasts. Further south, at 24°S, where the mantle wedge is characterized by low v_p and low Q_p, and the slab appears to thicken above the Benioff Zone. We suggest that detachment has already been completed with the cold continental lithosphere resting atop the subducted Nazca plate (Fig. 11). The positive velocity anomaly of 6% to 8% can be explained by 500 to 700 °C difference in temperature (Sobolev et al., 1996). This is the difference between the cold lithosphere (800 °C) and hot asthenosphere (1300 °C). The contrast can be enhanced by chemical differences (e.g. higher Mg content in the lithosphere) or due to partial melts in the asthenospheric mantle wedge, which is supported by high v_p/v_s ratios found there (Fig. 5).

In contrast to pure thermal models (e.g., Houseman et al., 1981), cold lithosphere is not gravitationally unstable per se. In particular, the density of depleted lithosphere is lower than that for primitive mantle. This compositional variation may exceed the effect of thermal expansion and make lithosphere generally buoyant (Kay and Kay, 1993). Yet, the underlying asthenosphere is likely to contain significant amounts of partial melts, because water from the slab causes flux melting. This is supported by high v_p/v_s ratios and large, low Q_p regions observed in the mantle wedge in this study. Presence of melts reduces density and viscosity, allowing for the observed gravitational instability.

We interpret the low v_p and Q_p anomalies engulfing the detached lithosphere as expressions of viscous heating and decompressional melting due to rapid influx and ascent of hot asthenospheric mantle (Schott et al., 2000) (Fig. 11). Hot, fresh mantle at the base of the crust probably causes partial melting in the lower crust, responsible for the penetrating "hot" anomalies observed there. We also see very low P velocities in the upper-most crust and large positive station corrections for Q_p, pointing to a shallow low Q_p anomaly. Extensive shallow low velocity zones in the backarc crust have also been detected with teleseismic receiver-functions (Chmielowski et al., 1999; Yuan et al., 2000). They were interpreted as large regions of melt accumulation that may serve as sources for the large ignimbrite fields that have erupted in the backarc since the Miocene. Lithospheric detachment might be the ultimate heat source in the mantle that triggers large-scale crustal melting and widely observed felsic volcanism (Fig. 11).

Kay and Kay (1993) and Kay et al. (1994) proposed loss of the lithospheric lid at around 26°S, just south of our study area, based on low Q_p mantle (Whitman et al., 1992) and eruptions of ocean-island-type basalts and calc–alkaline lavas 1 to 2 Ma ago. Shoshonitic lavas, thought to have a lithospheric mantle source, are found up to 24°S, the southern limit of our detachment event. At 24°S, above a zone of low velocity and high attenuation in crust and mantle (Figs. 10 and 11) stands the Quaternary strato-volcano Cerro Tuzgle. In its vicinity, shoshonites as well as ocean-island-type basalts and ignimbrites occur (Coira and Kay, 1993). We believe that this volcanism is the result of a recent detachment of lithosphere, the remains of which are now lying on top of the Nazca plate. The shoshonitic, ocean-island-type, and ignimbrite lavas probably accompanied detachment. The youngest, andesitic lavas can be subduction related, due to fluids released into the now hot asthenospheric mantle from the vigorous earthquake cluster 200 km below. Because there is no mantle lid left, magmas can reach the surface, as they do 200 km to the west, in the volcanoes of the present volcanic arc.

There are further arguments for loss of lithosphere beneath the Puna. The Puna plateau has an average elevation of 4.5 km, almost 1 km higher than the Altiplano to the north. Yet new estimates for Moho depth from receiver-functions (Yuan et al., 2000) indicate significantly thinner crust for the Puna (~55–60 km vs. ~70 km for the Altiplano). In addition, shortening estimates from cross-sectional balancing for the Puna are consistently lower than they are to the north for the Altiplano (Kley and Monaldi, 1998). Grier et al. (1991) can explain only 30% of the crustal cross-sectional area due to tectonic shortening in the Puna. Some of the missing material may be explained through

lateral flux of crust in the thermally weakened middle and lower crust (Hindle et al., 2005).

Considering that the magnitude of lithospheric shortening across the Altiplano is much greater than that across the Puna, the Altiplano seems a likelier place for detachment to occur. Nonetheless, under the Altiplano a lithospheric lid appears to be still present (Whitman et al., 1992; Myers et al., 1998; Haberland et al., 2003), whereas beneath the Puna, lithosphere has been, or is in the process of being completely removed. These two provinces are also distinguished by different styles of upper crustal foreland deformation (Whitman et al., 1996). Allmendinger and Gubbels (1996) interpret the thin-skinned deformation of the Altiplano foreland as indicative of a simple-shear mode of lithospheric shortening, and the thick-skinned deformation of the Puna and its foreland as an expression of pure-shear shortening. This means that beneath the Altiplano, strong Brazilian lithosphere may currently be underthrust as a whole, intact plate. In contrast, beneath the Puna shortening of the lithosphere is distributed over the entire plateau (Klotz et al., 2001). Allmendinger and Gubbels (1996) also note that the pure shear and simple shear modes of shortening are sequential stages in plateau growth. Before the current simple shear mode of deformation, the southern Altiplano has undergone a stage of plateau-wide distributed shortening between 47 Ma and 8 Ma (Elger et al., 2005) that is highly similar to the current situation in the Puna. Our tomographic images are merely a snapshot of a transient state. Deformation in the Puna started much later (29 Ma) compared to the Altiplano. Because the Altiplano and the Puna are at different stages in the in the plateau-building process, a hypothetical tomographic experiment conducted in the late Miocene in the Altiplano may have produced a picture similar to the results obtained in this study. It is highly likely that the Altiplano has also lost mantle lithosphere during its earlier stage of pure shear shortening. The lack of a lithospheric root as well as the very high surface heat flow point to this, and the period of pronounced magmatism on the Altiplano plateau between 22 Ma and 7 Ma years might frame the timing. New lithosphere beneath the Altiplano might have been formed by underthrusting of Brazilian shield and "freezing on" of asthenospheric mantle.

5. Conclusions

The three parameters v_p, v_p/v_s and Q_p derived by local earthquake tomography in this study provide a consistent picture of the southern central Andes from forearc to backarc. The tomographic model reveals a seismically soft Andean plateau characterized by low velocities and high seismic attenuation in crust and mantle that is clamped between a seismically strong and cold forearc and likewise foreland. New data from the Puna plateau reveals intriguing structural details in the mantle wedge. A fast, high Q_p body dipping westward from beneath the Eastern Cordillera into the mantle wedge under the eastern Puna might be a rare observation of lithospheric detachment accompanying the plateau building process. A strong anomaly with low velocities and low Q_p in crust and mantle is found beneath the back arc volcano Cerro Tuzgle. Here lithosphere might have just been lost in a similar process as is indicated by recent, characteristic volcanism. Plateau formation in the central Andes might go through two distinct stages: (1) distributed, pure shear shortening of the entire lithosphere that leads eventually to lithospheric detachment. (2) Simple shear overthrusting of the plateau onto the stiff, strong foreland. The Puna is currently in stage 1 whereas the Altiplano is already in the more advanced stage 2.

Acknowledgments

We are thankful for the constructive comments of Dr. H. Thybo and two anonymous reviewers. This work was funded by the DFG through the SFB267. Instruments were provided by the Geophysical Instrument Pool Potsdam and Freie Universität Berlin. Thanks to all participants in the difficult and demanding field work that made the three experiments possible.

The views expressed herein are those of the authors and do not necessarily reflect the views of the CTBTO Preparatory Commission.

References

Allmendinger, R., Gubbels, T., 1996. Pure and simple shear plateau uplift, Altiplano–Puna, Argentina and Bolivia. Tectonophysics 259, 1–13.

ANCORP Working Group, 1999. Seismic reflections image revealing offset of Andean subduction-zone earthquake locations into oceanic mantle. Nature 397, 341–344.

Angermann, D., Klotz, J., Reigber, C., 1999. Space-geodetic estimation of the Nazca–South American Euler vector. Earth Planet. Sci. Lett. 171, 329–334.

Berckhemer, H., Kampfmann, W., Aulbach, E., Schmeling, H., 1982. Shear modulus and Q of forsterite and dunite near partial melting from forced-oscillation experiments. Phys. Earth Planet. Inter. 29, 30–41.

Bird, P., 1979. Continental delamination and the Colorado plateau. J. Geophys. Res. 84, 7561–7571.

Boyd, S., Jones, C.H., Sheehan, A.F., 2004. Foundering lithosphere imaged beneath the southern Sierra Nevada, California, USA. Science 305, 660–662.

Cahill, T.A., Isacks, B.L., 1992. Seismicity and the shape of the subducted Nazca Plate. J. Geophys. Res. 97 (B12), 17503–17529.

Chmielowski, J., Zandt, G., Haberland, C., 1999. The central Andean Altiplano–Puna magma body. Geophys. Res. Lett. 26, 783–786.

Coira, B., Kay, S.M., 1993. Implications of Quaternary volcanism at Cerro Tuzgle for crustal and mantle evolution of the Puna Plateau, central Andes. Contrib. Mineral. Petrol. 113, 40–58.

de Silva, S, 1989. Altiplano–Puna volcanic complex of the central Andes. Geology 17, 1102–1106.

Eberhart-Phillips, D., 1986. Three-dimensional structure in northern California coast ranges from inversion of local earthquake arrival times. Bull. Seismol. Soc. Am. 76, 1025–1052.

Eberhart-Phillips, D., 1993. Local earthquake tomography: earthquake source regions. In: Iyer, H., Hirahara, K. (Eds.), Seismic Tomography: Theory and Practice. Chapman and Hall, London, pp. 613–643.

Eberhart-Phillips, D., Michael, A.J., 1998. Seismotectonics of the Loma Prieta, California, region determined from three-dimensional v_p, v_p/v_s, and seismicity. J. Geophys. Res. 103, 21099–21120.

Elger, K., Oncken, O., Glodny, J., 2005. Plateau-style accumulation of deformation – the Southern Altiplano. Tectonics 24f (4). doi:10.1029/2004TC001675.

Engdahl, E., van der Hilst, R., Buland, R., 1998. Global teleseismic earthquake relocation with improved travel times and procedures for depth determination. Bull. Seismol. Soc. Am. 88, 722–743.

Evans, J., Eberhard-Phillips, D., Thurber, C.H., 1994. User's manual for simulps12 for imaging v_p and v_p/v_s: a derivative of the "Thurber" tomographic inversion simul3 for local earthquakes and explosions. Open File Report, vol. 94-431. U.S. Geological Survey.

Giese, P., Scheuber, E., Schilling, F., Schmitz, M., Wigger, P., 1999. Crustal thickening processes in the central Andes and the different natures of the Moho-discontinuity. J. South Am. Earth Sci. 12, 201–220.

Graeber, F., Asch, G., 1999. Three-dimensional models of P-wave velocity and P-to-S-velocity ratio in the southern central Andes by simultaneous inversion of local earthquake data. J. Geophys. Res. 104, 20237–20256.

Gregory-Wodzicki, K.M., 2000. Uplift history of the central and northern Andes. GSA Bull. 112, 1091–1105.

Grier, M.E., Salfity, J.A., Allmendinger, R., 1991. Andean reactivation of Cretaceous Salta rift northwestern Argentina. J. South Am. Earth Sci. 4, 351–372.

Haberland, C., Rietbrock, A., 2001. Attenuation tomography in the western central Andes: a detailed insight into the structure of a magmatic arc. J. Geophys. Res. 106, 11151–11167.

Haberland, C., Rietbrock, A., Schurr, B., Brasse, H., 2003. Coincident anomalies of seismic attenuation and electrical resistivity beneath the southern Bolivian Altiplano Plateau. Geophys. Res. Lett. 30 (18), 1923. doi:10.1029/2003GL017492.

Haslinger, F., Kissling, E., 2001. Investigating effects of 3-d ray tracing methods in local earthquake tomography. Phys. Earth Planet. Inter. 123, 103–114.

Hindle, D., Kley, J., Oncken, O., Sobolev, S., 2005. Crustal balance and crustal flux from shortening estimates in the central Andes. Earth Planet. Sci. Lett. 230, 113–124.

Houseman, G.A., McKenzie, D.P., Molnar, P., 1981. Convective instability of a thickened boundary layer and its relevance for thermal evolution of continental convergent belts. J. Geophys. Res. 86, 6115–6132.

Husen, S., Kissling, E., 2001. Local earthquake tomography of shallow subduction in north Chile: a combined onshore and offshore study. J. Geophys. Res. 105, 28183–28198.

Isacks, B., 1988. Uplift of the central Andean plateau and bending of the Bolivian orocline. J. Geophys. Res. 93, 3211–3231.

Jackson, I., Paterson, M.S., Fitzgerald, J.D., 1992. Seismic wave dispersion and attenuation in Aheim dunite: an experimental study. Geophys. J. Int. 108, 517–534.

James, D.E., 1971. Andean crustal and upper mantle structure. J. Geophys. Res. 76, 3246–3271.

Kay, R.W., Kay, S.M., 1993. Delamination and delamination magmatism. Tectonophysics 219, 177–189.

Kay, S.M., Coira, B., Viramonte, J., 1994. Young mafic back arc volcanic rocks as indicators of continental lithospheric delamination beneath the Argentine Puna plateau, central Andes. J. Geophys. Res. 99, 24323–24339.

Kay, S., Mpodozis, C., Coira, B., 1999. Neogene magmatism, tectonism, and mineral deposits of the central Andes (22 to 33 degrees S latitude). In: Skinner, B.J. (Ed.), Geology and Ore Deposits of the Central AndesSpecial Publication (Society of Economic Geologists, vol. 7, pp. 27–59.

Kennett, B.L.N., 1991. IASPEI 1991 Seismological Tables. Bibliotech, Canberra, Australia.

Kissling, E., Ellsworth, W., Eberhart-Phillips, D., Kradolfer, U., 1994. Initial reference models in local earthquake tomography. J. Geophys. Res. 99, 19635–19646.

Kley, J., Monaldi, C., 1998. Tectonic shortening and crustal thickness in the central Andes: how good is correlation? Geology 26, 723–726.

Klotz, J., Khazaradze, G., Angermann, D., Reigber, C., Perdomo, R., Cifuentes, O., 2001. Earthquake cycle dominates contemporary crustal deformation in central and southern Andes. Earth Planet. Sci. Lett. 193, 437–446.

Kosarev, G., Kind, R., Sobolev, S., Yuan, X., Hanka, W., Oreshin, S., 1999. Seismic evidence for detached lithospheric mantle beneath Tibet. Science 283, 1306–1309.

Menke, W., 1989. Geophysical Data Analysis: Discrete Inverse Theory. Academic Press, San Diego.

Michelini, A., McEvilly, T., 1991. Seismological studies at Parkfield: I. Simultaneous inversion for velocity structure and hypocenters using cubic B-splines parameterization. Bull. Seismol. Soc. Am. 81, 524–552.

Myers, S.C., Beck, S., Zandt, G., Wallace, T., 1998. Lithospheric-scale structure across the Bolivian Andes from tomographic images of velocity and attenuation for P and S waves. J. Geophys. Res. 103, 21.233–21.252.

Park, J., Lindberg, C.R., Vernon, F.L., 1987. Multitaper spectral analysis of high-frequency seismograms. J. Geophys. Res. 92, 12.675–12.684.

Parsons, B., Sclater, J.G., 1977. Analysis of the variation of ocean floor bathymetry and heat flow with age. J. Geophys. Res. 82, 803–827.

Pavlis, G., Booker, J.R., 1980. The mixed discrete–continuous inverse problem: application to the simultaneous determination of earthquake hypocenters and velocity structure. J. Geophys. Res. 85, 4801–4810.

Podvin, P., Lecomte, I., 1991. Finite difference computation of traveltimes in very contrasted velocity models; a massively parallel approach and its associated tools. Geophys. J. Int. 105, 271–284.

Peacock, S.M., 1996. Thermal and petrologic structure of subduction zones. In: Bebout, G., Scholl, D., Kirby, S., Platt, J. (Eds.), Subduction Top to Bottom. American Geophysical Union, pp. 119–133.

Prothero, W.A., Taylor, W., Eickemeyer, J.A., 1988. A fast, two-point, three-dimensional raytracing algorithm using a simple step search method. Bull. Seismol. Soc. Am. 78, 1190–1198.

Rietbrock, A., Entwicklung eines Programmsystems zur konsistenten Auswertung großer seismologischer Datensätze mit Anwendung auf die Untersuchung der Absorptionsstruktur der Loma-Prieta-Region, Kalifornien, Ph.D. thesis, LMU München, 1996.

Rietbrock, A., 2001. P wave attenuation structure in the fault area of the 1995 Kobe earthquake. J. Geophys. Res. 106, 4141–4154.

Rietbrock, A., Haberland, C., 1998. ANCORP'96: das passive seismologische experiment. Berichtsband für die Jahre 1996–1998Sonderforschungbereich 267: Deformationsprozesse in den Anden, pp. 470–479.

Schott, B., Schmeling, H., 1998. Delamination and detachment of a lithospheric root. Tectonophysics 296, 225–247.

Schott, B., Yuen, D., Schmeling, H., 2000. The significance of shear heating in continental delamination. Phys. Earth Planet. Inter. 118, 273–290.

Schurr, B., 2001. Seismic structure of the central Andean subduction zone from local earthquake data. Scientific Technical Report STR01/01. GeoForschungsZentrum, Potsdam.

Schurr, B., Rietbrock, A., 2004. Deep seismic structure of the Salar de Atacama basin, northern Chile. Geophys. Res. Lett. 31, L12601. doi:10.1029/2004GL019796.

Schurr, B., Asch, G., Rietbrock, A., Kind, R., Pardo, M., Heit, B., Monfret, T., 1999. Seismicity and average velocity beneath the Argentine Puna. Geophys. Res. Lett. 26, 3025–3028.

Schurr, B., Asch, G., Rietbrock, A., Trumbull, R., Haberland, C., 2003. Earth Planet. Sci. Lett. 215, 105–119.

Sobolev, S., Zeyen, H., Stoll, G., Werling, F., Altherr, R., Fuchs, K., 1996. Upper mantle temperatures from tomography of French Massiv Central including effects of composition, mineral reactions, anharmonicity, anelasticity, and partial melt. Earth Planet. Sci. Lett. 139, 147–163.

Springer, M., Förster, A., 1998. Heat-flow density across the central Andean subduction zone. Tectonophysics 291, 123–139.

Thurber, C., 1983. Earthquake locations and three-dimensional crustal structure in the Coyote Lake area, central California. J. Geophys. Res. 88, 8.226–8.236.

Thurber, C., Eberhart-Phillips, D., 1999. Local earthquake tomography with flexible gridding. Comput. Geosci. 25, 809–818.

Um, J., Thurber, C., 1987. A fast algorithm for two-point seismic ray tracing. Bull. Seismol. Soc. Am. 77, 972–986.

Whitman, D., Isacks, B., Chatelain, J.-L., Chiu, J.-M., Perez, A., 1992. Attenuation of high-frequency seismic waves beneath the central Andean plateau. J. Geophys. Res. 97, 19.929–19.947.

Whitman, D., Isacks, B.L., Kay, S.M., 1996. Lithospheric structure and along strike segmentation of the central Andean plateau: seismic *Q*, magmatism, flexure, topography and tectonics. Tectonophysics 259, 29–40.

Wigger, P.J., et al., 1994. Variation of the crustal structure of the southern central Andes deduced from seismic refraction investigations. In: Reutter, K.-J., Scheuber, E., Wigger, P.-J. (Eds.), Tectonics of the Southern Central Andes. Springer, Berlin, pp. 23–48.

Yuan, X., et al., 2000. Subduction and collision processes in the central Andes constrained by converted seismic phases. Nature 408, 958–961.